



UNIVERSITY OF LEEDS

This is a repository copy of *Lidar Observations of the Upper Atmospheric Nickel Layer at Beijing (40°N,116°E)*.

White Rose Research Online URL for this paper:

<https://eprints.whiterose.ac.uk/168822/>

Version: Accepted Version

Article:

Wu, F, Zheng, H, Yang, Y et al. (8 more authors) (2021) Lidar Observations of the Upper Atmospheric Nickel Layer at Beijing (40°N,116°E). *Journal of Quantitative Spectroscopy and Radiative Transfer*, 260. 107468. ISSN 0022-4073

<https://doi.org/10.1016/j.jqsrt.2020.107468>

©2020 Published by Elsevier Ltd. . Licensed under the Creative Commons Attribution-NonCommercial-NoDerivatives 4.0 International License (<http://creativecommons.org/licenses/by-nc-nd/4.0/>).

Reuse

This article is distributed under the terms of the Creative Commons Attribution-NonCommercial-NoDeriv (CC BY-NC-ND) licence. This licence only allows you to download this work and share it with others as long as you credit the authors, but you can't change the article in any way or use it commercially. More information and the full terms of the licence here: <https://creativecommons.org/licenses/>

Takedown

If you consider content in White Rose Research Online to be in breach of UK law, please notify us by emailing eprints@whiterose.ac.uk including the URL of the record and the reason for the withdrawal request.



eprints@whiterose.ac.uk
<https://eprints.whiterose.ac.uk/>

Lidar Observations of the Upper Atmospheric Nickel Layer at Beijing (40° N, 116° E)

Fuju Wu^{1,2}, Haorang Zheng¹, Yong Yang³, Xuewu Cheng³, Faquan Li³, Lifang Du¹, Jihong Wang¹, Jing Jiao¹, John M.C. Plane⁴, Wuhu Feng⁵, and Guotao Yang^{1,*}

¹State Key Laboratory of Space Weather, National Space Science Center, Chinese Academy of Sciences, Beijing, 100190, China

²University of Chinese Academy of Sciences, Beijing 100049, China

³State Key Laboratory of Magnetic Resonance and Atomic and Molecular Physics, Wuhan Institute of Physics and Mathematics, Chinese Academy of Sciences, Wuhan, 430071, China

⁴School of Chemistry, University of Leeds, Leeds, UK

⁵National Centre for Atmospheric Science (NCAS), University of Leeds, Leeds, UK

*Corresponding author: gtyang@nssc.ac.cn

Abstract: Ni atoms, produced in the Earth's upper atmosphere by meteoric ablation, are challenging to measure by lidar because the Ni atom density is low, the resonance scattering cross section is relatively small, and the transitions occur in the near-UV around 340 nm where absorption by the stratospheric ozone layer starts to become significant. A new Ni lidar has been designed and deployed at Yanqing station (40° N, 116° E) Beijing, China over the period from 3 April 2019 to 31 December 2019. The combination of a frequency-doubled near-IR laser and narrow bandwidth filters enables stable and continuous operation. From 25 nights of measurements, the Ni peak density ranges from 98 to 460 cm⁻³ with the peak altitude between 80 and 88 km; the average peak density is 258 ± 115 cm⁻³. The average column abundances of Nickel varied between 1.52 × 10⁸ and 6.0 × 10⁸ cm⁻² between mid-summer and mid-winter. An experiment was also carried out using the Ni lidar to determine the spectroscopic branching ratios from the excited Ni(³F₄) state into 3 lower

1 states; very close agreement with the literature values were obtained

2 **Key words:** Nickel lidar; meteoric metals; mesosphere; Ni atomic
3 spectroscopy.

4 **1. Introduction**

5 The ablation of cosmic dust particles entering the Earth's atmosphere
6 produces layers of metal atoms in the mesosphere and lower thermosphere
7 region (MLT) from 80 to 110 km [1]. The metal layers are very useful
8 tracers of atmospheric dynamics (e.g., gravity waves and tides) [2-4], and
9 also of coupling between the neutral atmosphere and ionosphere [5-7]. The
10 resonance lidar is a powerful tool for detecting the metal layers with
11 excellent spatial and temporal resolution (Na at 589 nm, K at 770 nm, Fe
12 at 372 nm, and Ca at 423 nm) [8-10]; Due to the large resonance scattering
13 cross section and relatively high concentration of Na atoms, the sodium
14 lidar was the first resonance lidar to be developed [11]. Subsequently, the
15 Na layer has been extensively studied all over the world by lidar [1,12-15].
16 Lidar studies of other metals such as K, and Ca are more challenging,
17 because their abundance is low in the MLT region. Nevertheless, extensive
18 measurements of these metals have also been made [1], including the
19 seasonal variations of the K layer[16,17], sporadic Ca layers [18,19], and
20 the recent discovery of thermospheric K layers [20,21].

21 Nickel is one of the most challenging metal atoms to detect in the
22 MLT because the backscatter cross section of Ni atoms is relatively small

1 (i.e., 6-30 times lower than the Na backscatter cross section). So far, there
2 are only two reported lidar observations of the Ni layer. Collins et al. [22]
3 made the first measurements by lidar at Chatanika, Alaska ($65^{\circ}\text{N}, 147^{\circ}\text{W}$)
4 in 2015. They used a lidar operating at 337 nm, and reported the peak
5 density of the Ni layer to be $1.6 \times 10^4 \text{ cm}^{-3}$ at ~ 87 km. Subsequently,
6 Gerding et al. [23] conducted six nights of lidar observations at K \ddot{u}
7 hlungsborn, Germany ($54^{\circ}\text{N}, 12^{\circ}\text{E}$). They used resonance transitions at
8 both 341 nm and 337 nm to detect Ni. The mean peak density of the Ni
9 layer they obtained was only between 280 and 450 cm^{-3} .

10 Unlike metal atoms such as Na and K, when Ni is pumped up to a
11 low-lying electronically excited state emission can occur to several lower
12 states including the ground ($^3\text{F}_4$) state [22, 23]. The branching ratios for
13 fluorescence into these lower states can be measured in a high altitude lidar
14 experiment (where quenching by air molecules is much slower than
15 emission), and compared with theoretical values from atomic physics.

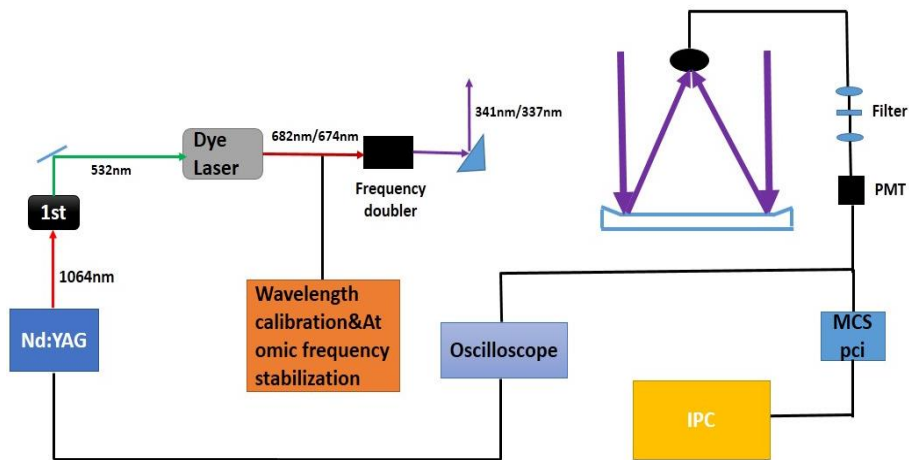
16 In this paper, we report the first observations of the Ni layer at the
17 Yanqing Station ($40^{\circ}\text{N}, 116^{\circ}\text{E}$) of the Chinese Meridian Project [24].
18 Section 2 describes the dye lidar system, which employs frequency
19 doubling technology to produce laser light at 341 or 337 nm. Section 3
20 describes the inverse method used to determine the absolute Ni density. In
21 Section 4 we present 25 nights of Ni observations. Section 5 describes the
22 measurement of the spectroscopic branching ratios of Ni over different

1 transition lines. Section 6 contains a discussion of the results, and
2 conclusions.

3 2. Lidar system and Technical advantages

4 2.1 Lidar system

5 Figure 1 is a schematic diagram of the dual-wavelength lidar system
6 to measure Ni, developed at the Yanqing Station (40° N, 116° E).



7
8 Figure 1. Schematic diagram of the Ni lidar system.

9 The Nd:YAG fundamental laser beam at 1064 nm is frequency-
10 doubled (LBO doubling crystal) to generate 532 nm laser radiation with a
11 pulse energy of 520 mJ. This is used to pump a VISTA dye laser with LDS
12 698 dye to produce an infrared laser beam at 683.1487 nm (in vac.) or
13 674.1062 nm (in vac.), before frequency-doubling to the Ni resonance
14 transitions at 341.5744 nm (in vac.) or 337.0531 nm (in vac.). The former,
15 with 17 mJ per pulse, corresponds to the Ni($^3D_3 \rightarrow ^3F_4$) transition. The
16 latter, with 15 mJ per pulse, corresponds to the Ni($^3F_4 \rightarrow ^3D^0$) transition. A
17 HighFinesse WS6-200 wavemeter is used to monitor the infrared
18 wavelength in real time and the automatic frequency stabilization software

1 stabilizes the infrared wavelength within 0.3 pm. In addition, we use
2 HighFinesse WS7 UVI wavemeter (with the function of measuring spectral
3 bandwidth) to measure the Ni resonance laser linewidth.

4 For the receiver, a reflecting telescope with a diameter of 1230 mm is
5 used to receive backscattered photons from the atmosphere (due to
6 Rayleigh elastic scattering and resonance fluorescence from Ni). The
7 telescope has a reflectivity greater than 95% at 341 nm and 337 nm. The
8 backscattered photons are directed first through a quartz fiber with a length
9 of 1 m and a diameter of 1.5 mm, and then a collimating lens. The photons
10 then pass through optical interference filter to reduce stray light. Two
11 optical interference filters are used in the receiver. One is an ALLUXA
12 OD5 narrowband filter with a FWHM (full width at half maximum) of 4
13 nm and 93% transmission, which is used in 341 nm channel. And the other
14 is an ALLUXA OD6 narrowband filter used in 337 nm channel with a
15 FWHM of 5 nm and ~75% transmission. The detector is a H10682-210
16 photomultiplier (PMT).

17 For data acquisition we use a photon-counting multichannel scaler
18 system (MCS-pci data acquisition card) to collect time-resolved data. The
19 raw data files are stored with a spatial resolution of 96 m (corresponding
20 to a channel bin width of 640 ns), and accumulated for 33 s. The system
21 parameters of the Ni lidar are listed in Table 1.

22 Table. 1. The system parameters of the Ni lidar

Transmitter

Wavelength	341.5744 nm (vac.) 337.0531 nm (vac.)
Pulse energy	17 mJ (341.5744 nm) 15 mJ (337.0531 nm)
Linewidth	0.9547 GHz
Repetition rate	30 Hz
Beam divergence	0.21 mrad

Receiver

Telescope diameter	1.23 m
Focal length	2.4 m
Field of view	0.625 mrad
PMT	H10682-210
Quantum efficiency of PMT	<40%
Filter bandwidth	4 nm (OD5) 5 nm (OD6)
IF transmittance	~93% (341 nm) ~75% (337 nm)

Data acquisition

Temporal resolution	33 s
Vertical spatial resolution	96 m

1 2.2 Technical advantages

2 As mentioned above, the two earlier lidars used excimer-pumped dye
3 lasers to detect the Ni layer. The excimer pump laser emits 308 nm light to
4 pump the dye laser, which then produces the Ni resonance wavelength.
5 There are two disadvantages with such a system: first, the UV excimer
6 beam rapidly destroys the dye molecules, so that the dye needs to be
7 replaced every few hours; second, UV laser dyes have a comparatively low
8 conversion efficiency. Hence, the excimer-pumped dye laser system is not
9 favorable for making continuous Ni measurements over long periods. In
10 contrast, the system used here employs 532 nm laser light to pump a near-
11 IR laser dye with a high conversion efficiency and long life (dye

1 replacement every 36 hours; the oscillator of the dye laser uses 0.042 g
2 LDS 698 dissolved in 500 ml ethanol, the amplifier of the dye laser uses
3 0.045 g LDS 698 dissolved in 1000 ml ethanol), which is much better
4 suited to long-term observations. A further advantage is that frequency-
5 doubling the IR laser beam avoids the disturbances by Amplified
6 Spontaneous Emission (ASE). This relatively broadband emission, some
7 of which is outside the narrow laser line used to excite resonance
8 fluorescence from Ni, is still Rayleigh back-scattered. This means that the
9 Rayleigh signal, which is used to calibrate the absolute Ni density (see
10 below), is enhanced, leading to an underestimate of the Ni density.
11 However, frequency-doubling the dye laser beam greatly reduces the ASE
12 contribution away from the center wavelength, because the doubling
13 efficiency is non-linear.

14 Switching the wavelength of the near-IR laser beam between
15 683.1487 nm and 674.1062 nm, and hence the two resonance wavelengths
16 (341.5744 nm and 337.0531 nm), is achieved by scanning the position of
17 the dye laser grating. This takes about 8 minutes, during which it is
18 assumed that the Ni density profile does not change significantly. This
19 assumption was tested (see below). Finally, as stated above the dye laser
20 wavelength is stabilized within a range of 0.3 pm so that, after frequency-
21 doubling, the Ni resonance wavelength has an error of only 0.15 pm.

22 A final advantage of this new Ni lidar is the use of narrow bandwidth

1 interference filters (see above), which are much narrower than the 29 nm
 2 bandwidth filter used by Gerding et al. [23]. The narrow bandwidth filters
 3 better discriminate against background light. This improves the SNR of the
 4 lidar signal, which is essential when detecting the relatively weak signal
 5 from the Ni layer. The Ni lidar system at the Yanqing station was therefore
 6 designed to improve the detectability of the Ni layer in a number of ways,
 7 compared with the two previous studies [22, 23].

8 **3. Inversion method**

9 The absolute Ni density is derived using the standard lidar equation
 10 (e.g. Megie et al. [25], Chu and Papen [26], Gerding et al. [23]):

$$11 \quad \mathbf{n}_{\text{Ni}} = \mathbf{n}_r \frac{\mathbf{N}_s - \mathbf{N}_b}{\mathbf{N}_r - \mathbf{N}_b} \frac{\mathbf{z}^2}{\mathbf{z}_r^2} \frac{\sigma_r}{\sigma_{\text{eff}}} \frac{1}{\mathbf{R}_B} \quad (1)$$

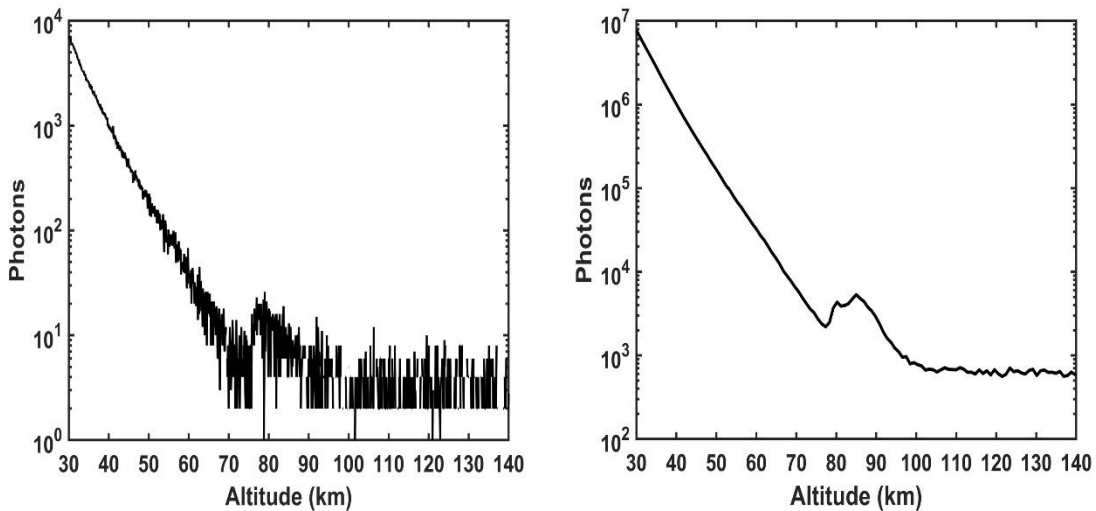
12 where, \mathbf{n}_{Ni} is the Ni number density; \mathbf{n}_r is the atmospheric total number
 13 density at the reference altitude, given by the NRLMSISE-00 model [27];
 14 σ_r is the Rayleigh backscatter cross section at the reference altitude \mathbf{z}_r
 15 (selected as 40 km); and σ_{eff} is the effective backscatter scattering cross
 16 section. At 341.5744 nm, $\sigma_r = 3.55 \times 10^{-31} \text{ m}^2 / \text{sr}$ and $\sigma_{\text{eff}} = 1.58 \times 10^{-17}$
 17 m^2 / sr ; and at 337.0531 nm $\sigma_r = 3.74 \times 10^{-31} \text{ m}^2 / \text{sr}$ and $\sigma_{\text{eff}} = 3.14 \times 10^{-18}$
 18 m^2 / sr . \mathbf{N}_s and \mathbf{N}_r are the number of echo photons received by the
 19 telescope at the altitude \mathbf{z} and at the reference altitude \mathbf{z}_r , respectively,
 20 and \mathbf{N}_b is the combination of altitude independent PMT dark count rate
 21 and stray light signal with the altitude dependent Rayleigh background

1 signal superimposed on the resonance signal (see section 4); and \mathbf{R}_B is
2 the branching fraction. Combining the parameters of Table 2 and the
3 bandwidth of the filter, the branching fraction \mathbf{R}_B can be determined (see
4 section 5 for details).

5 **4. Results**

6 **4.1 Detection of Ni at 341.5744 nm and at 337.0531 nm**

7 Collins et al. [22] measured Ni at 337 nm, and Gerding et al. [23] then
8 showed that a much better signal was obtained at 341 nm. Here we describe
9 measurements made at both wavelengths over the Yanqing station.



10

11

Figure 2. Left panel: raw backscatter signal at 341.5744 nm on the night of April 2, 2019, obtained from 1000 laser
12 shots in 33 s. Right panel: integrated backscatter signal for 1 hour (Spatial resolution is 960 m).

12

13

Ni was initially detected at 341.5744 nm on the night of 2 April 2019.

14

Figure 2 (left panel) shows the raw backscatter signal detected from 1000

15

laser pulses. This shows that the resonance backscatter from Ni above 70

16

km is small, and the peak of the Ni layer is equivalent to the Rayleigh echo

17

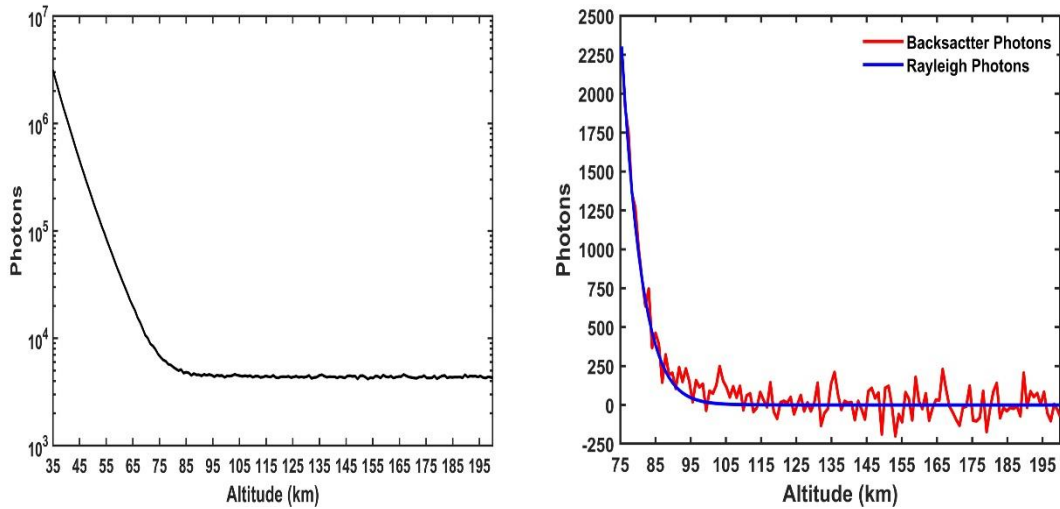
signal at about 65 km. However, this is the signal obtained in only 33 s.

18

The SNR is much improved by integrating the raw data files over one hour

1 (Figure 2 (right panel)). More than 5000 photons have now been
2 accumulated at the layer peak at 85 km, compared with less than 1000
3 photons of noise. Hence, the SNR exceeds 3, establishing the ability of the
4 new Ni lidar system for detecting Ni atoms at 341.5744 nm.

5 In order to determine whether the PMT has Signal-Induced Noise
6 (SIN) [28], we shifted the laser wavelength by 100 pm to 341.4744 nm and
7 collected signal for two hours data (Figure 3 (left panel)). For the lidar
8 signal, we first deduct the background noise (PMT dark count and stray
9 light signal) and then use the NRLMSISE-00 density profile [27] to
10 extrapolate the echo photons above 75 km (Figure 3 (right panel)). It can
11 be concluded from Figure 3 that there is almost no SIN. However, there are
12 often some photons that could not be attributed to Ni signal above 100 km.
13 For situations where the signal or noise cannot be distinguished, we
14 calculate the detection limit (mean background photon noise plus 1.5 times
15 its standard deviation) according to the method of Gao et al. [29] (shown
16 in Figure 4). When calculating the Ni density, the data below the detection
17 limit are not considered.



1

2

3

4

Figure 3. Left panel: lidar signal at 341.4744 nm. Right panel: lidar echo signal after removing the background noise (PMT dark count and stray light signal) and extrapolate the echo photons by the NRLMSISE-00 density profile. Time resolution is 120 min, spatial resolution is 960 m.

5

6

7

8

9

10

11

12

13

14

15

16

17

18

Figure 2 shows that there is potentially a small amount of Rayleigh backscatter signal in the resonance backscatter signal at the height of the Ni layer, which may affect the Ni density. In order to correct for this, the Rayleigh backscatter signal above 75 km was estimated by extrapolating the NRLMSISE-00 density profile [27] (Figure 4). In the Ni density calculation (Equation (1)), the extrapolated Rayleigh signal is subtracted together with the PMT dark count and stray light signal.

12

13

14

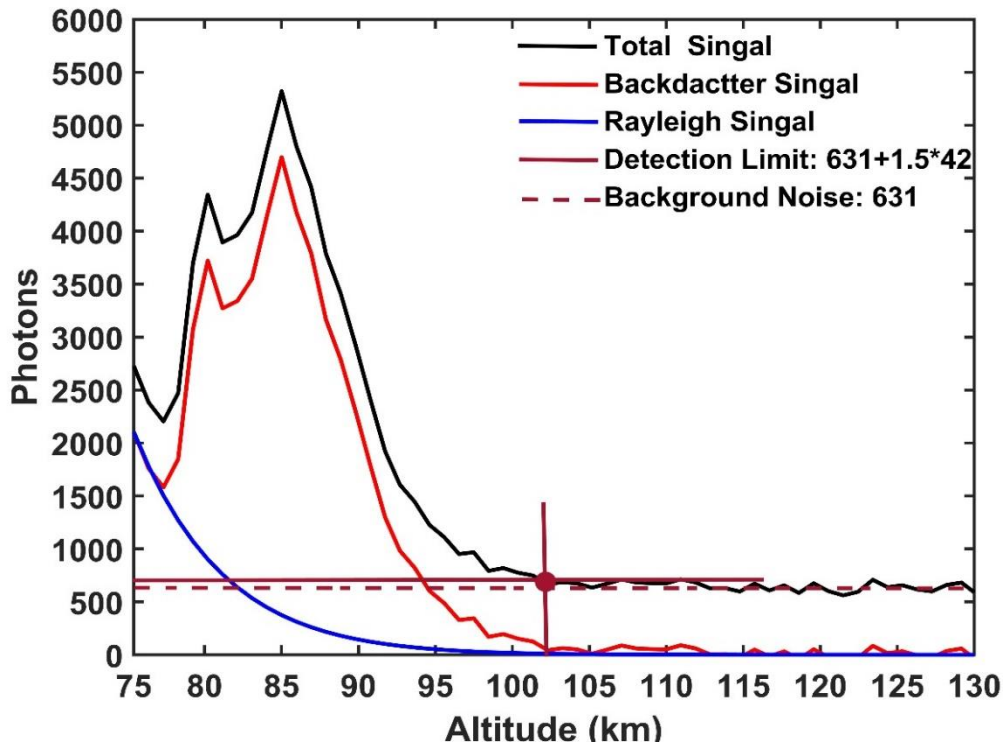
15

16

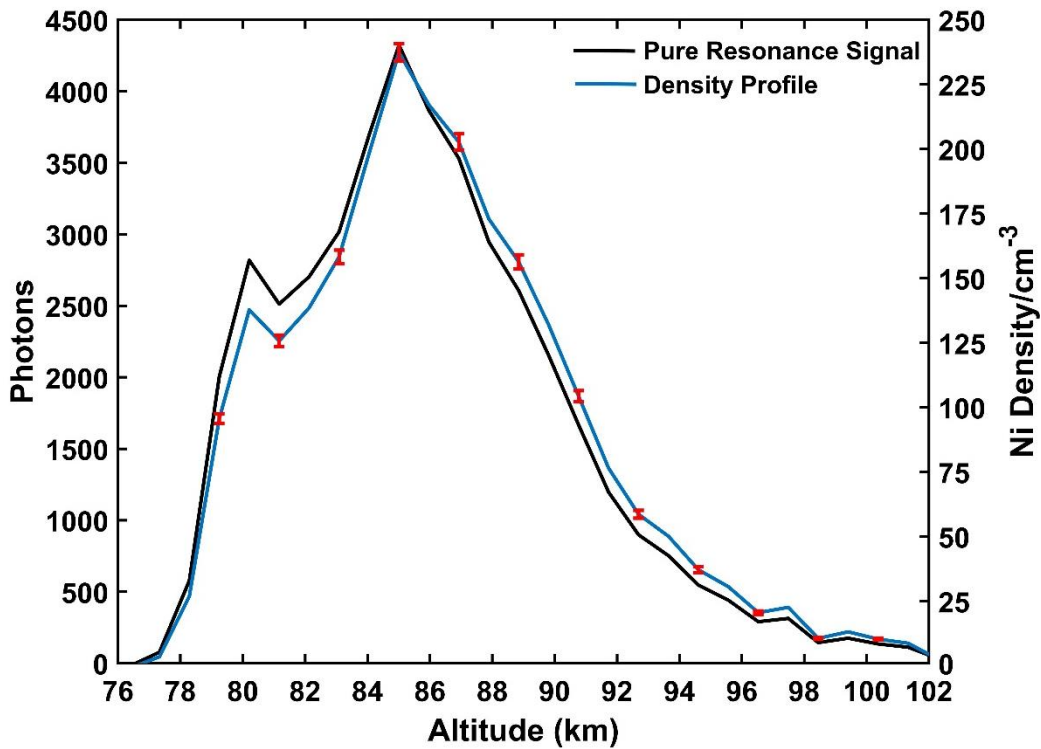
17

18

Figure 5 presents the pure resonance signal after subtracting the Rayleigh signal and background noise. The corresponding Ni concentration, calculated using Equation (1), is shown in Figure 5. The Ni layer is 77 km ~102 km with a peak concentration of 240 cm^{-3} at 85 km. There is the second small peak density around 80 km (corresponding the peak photon numbers in Figure 5). This result is similar to the observations made at 54°N in late winter by Gerding et al. [23].



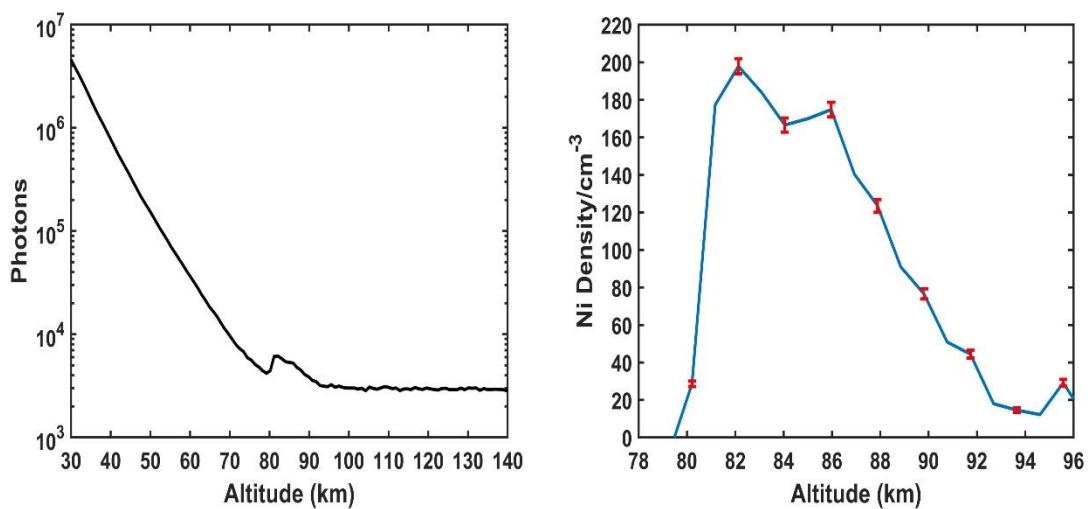
1
 2 Figure 4. Calculating the detection limit and extrapolating the Rayleigh signal for the signal of Figure 2 (right panel).
 3 Time resolution is 60 min, spatial resolution is 960 m.



4
 5 Figure 5. Pure resonance signal and the density profile from the pure resonance signal (error bars from photon
 6 statistics). Time resolution is 60 min, spatial resolution is 960 m. Recorded on April 2, 2019.

7 Ni was also successfully observed at 337 nm. It should be noted that
 8 the SNR of the lidar backscatter at 337.0531 nm is relatively poor because

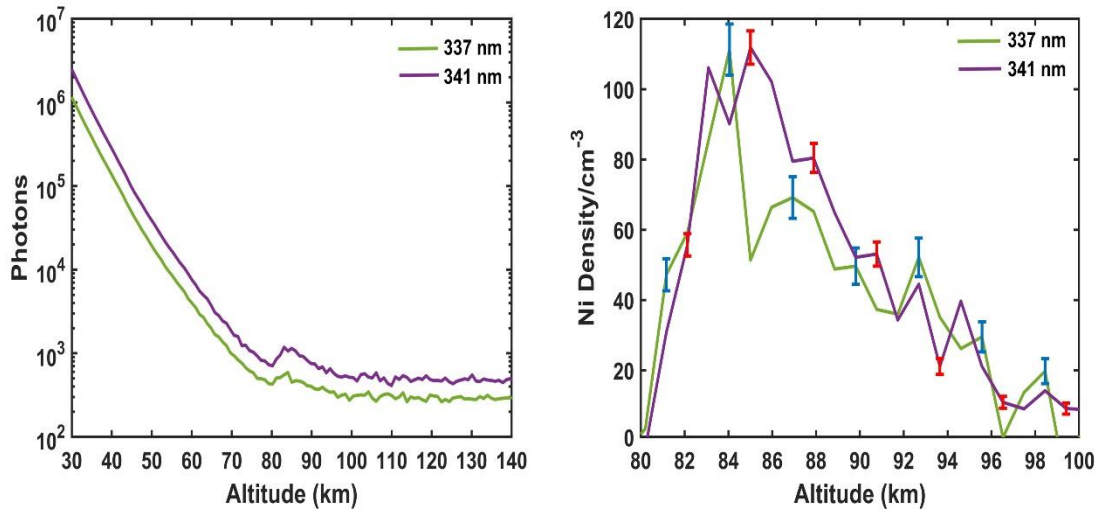
1 the OD6 interference filter is broader and only has 75% transmission, and
 2 the laser pulse energy is weaker (Table 1). Nevertheless, a good Ni
 3 backscatter signal was obtained by integrating 108,000 laser pulses, i.e.,
 4 one hour as shown in Figure 6. Similar to Figure 5, the observed Ni layer
 5 was in the height range 78~96 km, with a smaller peak density ($\sim 200 \text{ cm}^{-3}$)
 6 and a peak altitude that is 2~3 km lower.



7
 8 Figure 6. Left panel: integrated echo signal of the nickel atom layer on May 9, 2019. Right panel: the density
 9 profile from the integrated echo signal (error bars from photon statistics). Time resolution is 60 min, spatial
 10 resolution is 960m.

11 Following this initial success, an experiment was conducted on 28
 12 November 2019 of uninterrupted observations at the two Ni wavelengths.
 13 Ni was first measured from 15:17 to 16:17 UTC at 337.0531 nm, and then
 14 from 16:25 to 17:25 UTC at 341.5744 nm. Figure 7 compares the photon
 15 signals and retrieved Ni densities. Clearly, the SNR of the backscatter
 16 signal at 337.0531 nm is much smaller than that of 341.5744 nm, for the
 17 reasons discussed above. However, the retrieved Ni peak densities and
 18 peak altitudes are very similar, which confirms that the retrieved densities

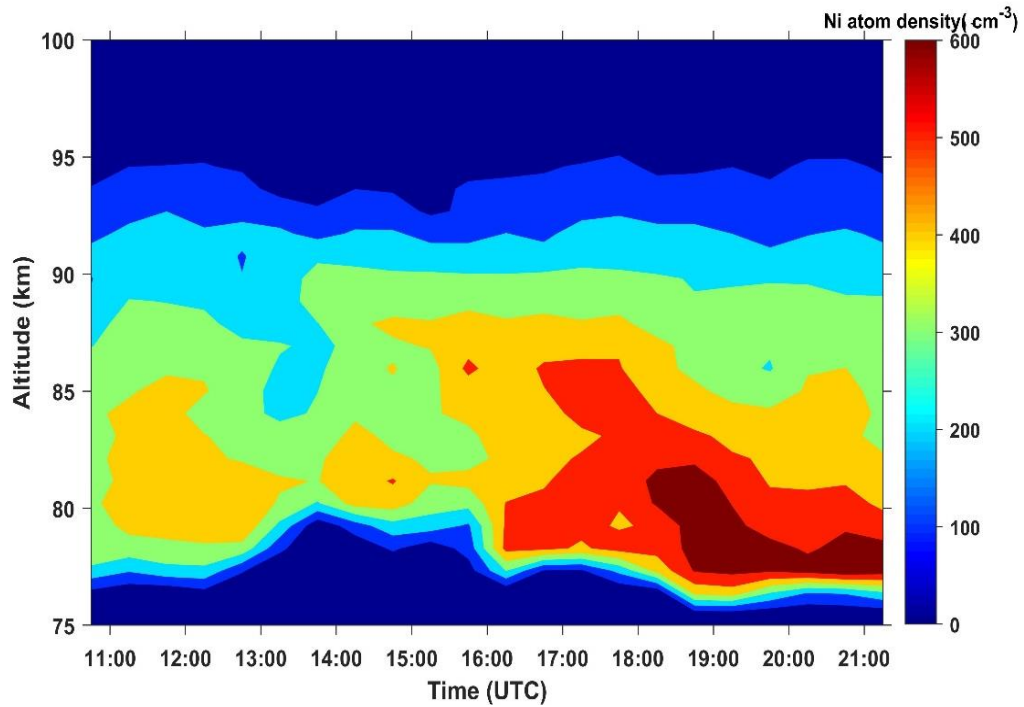
1 from observations at both wavelengths are robust.



2
3 Figure 7. Results of the uninterrupted wavelength comparison experiment. Left panel: backscatter signals detected
4 at the two resonance wavelengths. Right panel: the retrieved Ni density profiles. (Accumulation time is 60 min in
5 both bases, with a spatial resolution of 960 m; error bars from photon statistics).

6 **4.2 Night-time variability of the Ni layer**

7 The SNR of the backscatter signal obtained at 341 nm is significantly
8 better than at 337 nm, as shown in Section 4.1. We have selected 25 nights
9 (a total of 200.5 hours) with good coverage of Ni observations at 341 nm
10 where the SNR at the layer peak is > 3 . These nights are between 3 April
11 2019 and 31 December 2019. Figure 8 shows the night-time variation of
12 the Ni density from 11:00 to 21:00 UTC on December 5, 2019. The layer
13 extends from 76 to 95 km, with a peak density of 675 cm^{-3} at $\sim 80 \text{ km}$ after
14 18:00 UTC. Note the large change in the Ni peak density, from a minimum
15 of 392 cm^{-3} early in the night to a maximum of 675 cm^{-3} after 18:00 UTC.



1

2

Figure 8. The Ni density vertical profile versus time during the night of December 5, 2019. Time resolution is 30 min, spatial resolution is 960 m.

3

4

5

6

7

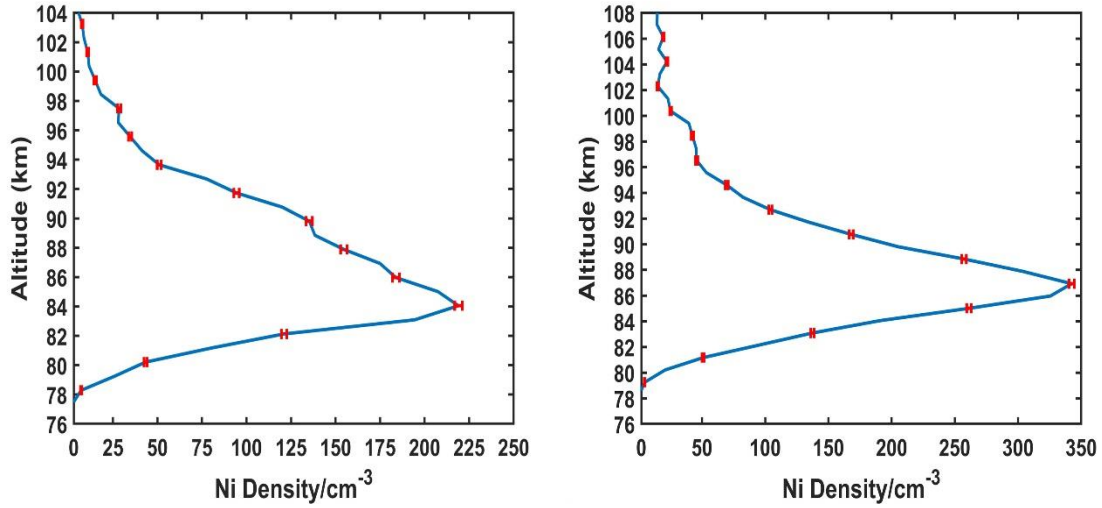
8

9

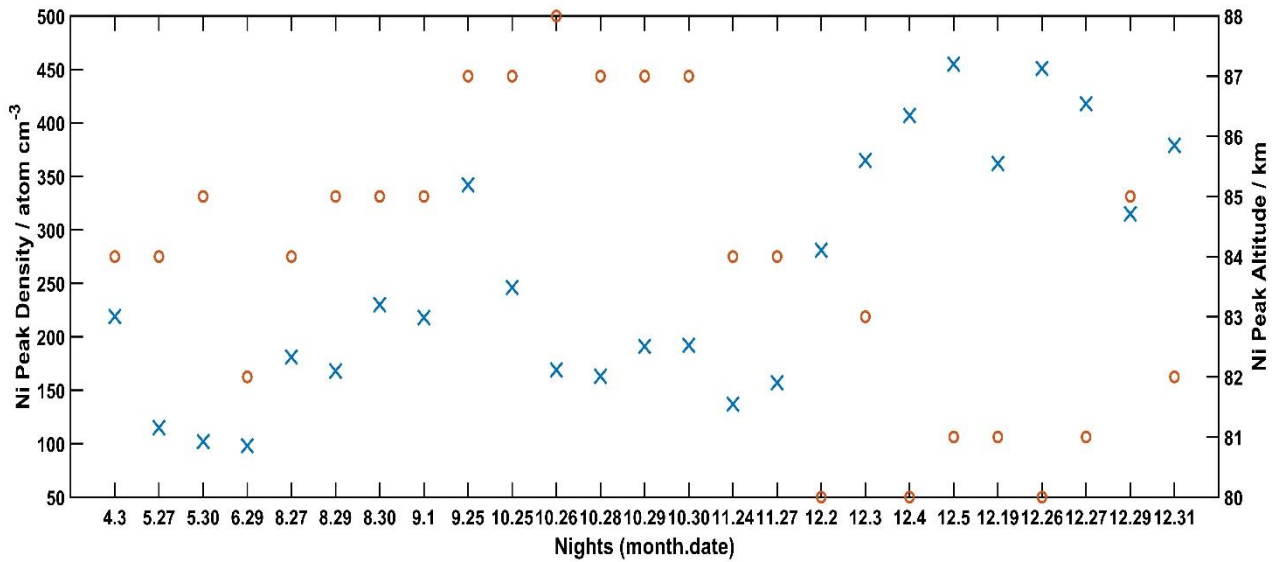
10

11

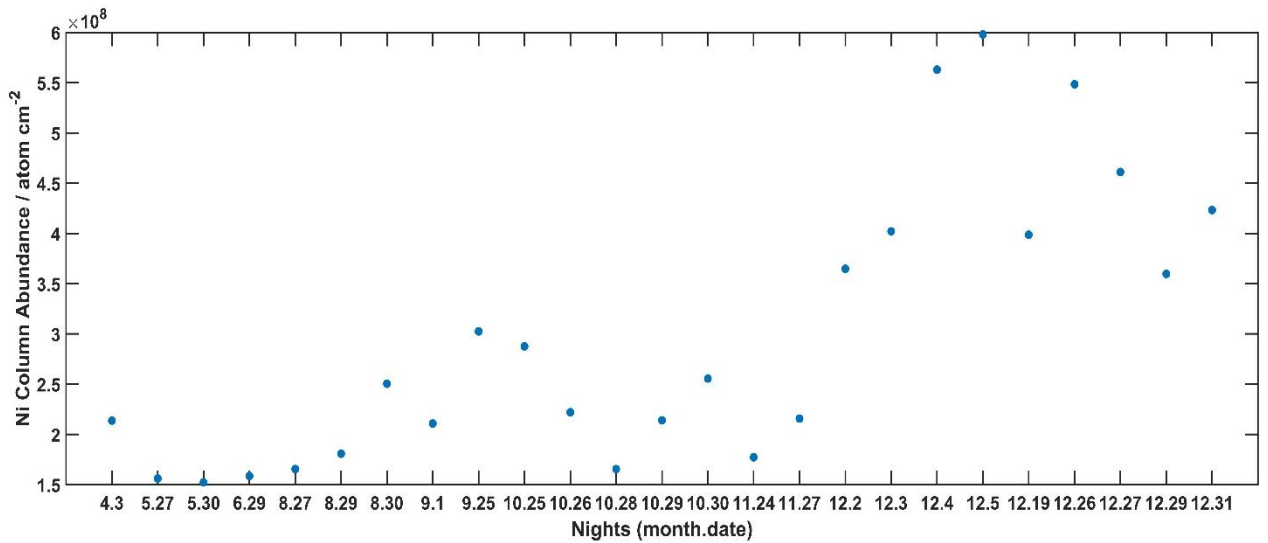
In order to compare seasonal variations, we calculated the nightly average Ni atom density profiles. Figure 9 shows two profiles (6 and 8.5 hours of data averaged) on 3 April and 25 September 2019. Both profiles exhibit a similar layer shape, with a peak density of 220 cm^{-3} at $\sim 84 \text{ km}$ on 3 April 2019 and $\sim 342 \text{ cm}^{-3}$ at 87 km on 25 September 2019. The FWHM of the layer on 3 April is 10.5 km and the FWHM of the layer on 25 September is 7 km. Note that the FWHM of the layer on 3 April is significantly broader than that on 25 September.



1
2 Figure 9. Average Ni density altitude profiles (error bars from photon statistics) on the nights of April 3, 2019 (left
3 panel) and September 25, 2019 (right panel).



4
5 Figure 10. Seasonal variation of the Ni atom nightly average peak density over 25 nights from date to date (The
6 small multiplication sign 'x' indicates the peak density, and the small circle 'o' indicates the peak altitude).



7

1 Figure 11. Seasonal variation of the Ni atom nightly average column abundance over 25 nights from date to date.

2 The seasonal variation of the peak density over 25 nights from April
3 – December, 2019, is shown in Figure 10. The maximum peak density of
4 $\sim 460 \text{ cm}^{-3}$ is observed in winter (on December 5, 2019), and the minimum
5 value of 98 cm^{-3} is observed in summer (June 29, 2019). The overall
6 average of the night peak density is $258 \pm 115 \text{ cm}^{-3}$. The nightly average
7 peak altitude varied from 80 km to 88 km.

8 Figure 11 shows the average column abundance during the 25 nights.
9 Similar to the peak density, the largest column abundance ($6.0 \times 10^8 \text{ cm}^{-2}$)
10 was observed on the night of December 5, and the smallest ($1.52 \times 10^8 \text{ cm}^{-2}$)
11 on May 30. The average from all the observations is $(3.0 \pm 1.4) \times 10^8$
12 cm^{-2} . The Ni data obtained so far indicates a maximum density in late
13 autumn and winter (October, November, and December), and a minimum
14 in May and August, though with large variability.

15 **5. Measurement of the Ni spectroscopic branching ratio**

16 As discussed in Section 3 and Gerding et al. [23], optically excited Ni
17 atoms can fluoresce to several lower energy states (this is unique among
18 the metals observed in the MLT by lidar). We therefore carried out a lidar
19 experiment to measure the branching ratios for Ni emission.

20 When the lidar operates at 341.5744 nm, Ni atoms in the low-lying
21 excited $3d^9(^2D)4s^3D_3$ state will be excited to the $3d^9(^2D)4p^3F_4$ state. Since
22 this Ni (3F_4) state is short-lived (lifetime = 16.19 ns; it is calculated from
23 the spectroscopic data published by Kramida et al. [30]), quenching by air

1 molecules will not occur before emission to 3 lower states: these are the
 2 $3d^9(^2D)4s^3D_3$, $3d^8(^3F)4s^2\ ^3F_4$ and $3d^8(^3F)4s^2\ ^3F_3$ states, corresponding to
 3 emission wavelengths of 341.5744 nm, 339.2016 nm and 355.2551 nm,
 4 respectively [30]. The branching ratio for Ni emission is given by [26]:

$$5 \quad \mathbf{BF}_{ki} = \mathbf{A}_{ki} \tau_k \quad (2)$$

6 where, \mathbf{BF}_{ki} is the branching ratio for transition from upper state k to low
 7 state i; \mathbf{A}_{ki} is the Einstein coefficient from level k to level i; and τ_k is
 8 the radiative lifetime of the state k.

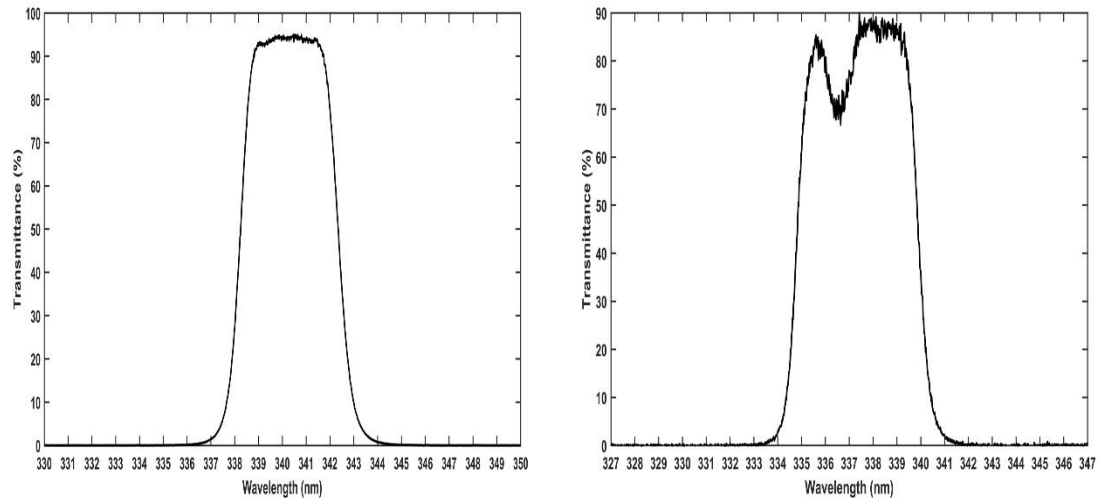
9 Similarly, the 337.0531nm laser excites Ni atoms in the $3d^8(^3F)4s^2\ ^3F_4$
 10 ground state to the $3d^9(^2D)4p^3D^o$ state. Emission from this excited state can
 11 occur to seven different lower states, with branching ratios that can be
 12 calculated using equation 2. The parameters of all these transitions are
 13 listed in Table 2 (The table lists parameters of the Ni spectroscopic
 14 transitions based on the spectroscopic data [30] and equation (2) [26]).

15 Table 2. Parameters of the Ni spectroscopic transitions

Absorption line ($3d^9(^2D)4s^3D_3 \rightarrow 3d^9(^2D)4p^3F_4$)				
Lower level	Upper level	Life-time	Wavelength	
$3d^9(^2D)4s^3D_3$	$3d^9(^2D)4p^3F_4$	16.19 ns	341.5744 nm(vac.)	
Transitions from $3d^9(^2D)4p^3F_4$				
Upper level	Lower level	Wavelength/ nm (vac.)	Einstein coefficient/ s^{-1}	Branching fraction
$3d^9(^2D)4p^3F_4$	$3d^9(^2D)4s^3D_3$	341.5744	5.5×10^7	0.8905
$3d^9(^2D)4p^3F_4$	$3d^8(^3F)4s^2\ ^3F_4$	339.2016	6.6×10^6	0.1069
$3d^9(^2D)4p^3F_4$	$3d^8(^3F)4s^2\ ^3F_3$	355.2551	1.6×10^5	0.0026
Absorption line ($3d^8(^3F)4s^2\ ^3F_4 \rightarrow 3d^9(^2D)4p^3D^o$)				
Lower level	Upper level	Life-time	Wavelength	
$3d^8(^3F)4s^2\ ^3F_4$	$3d^9(^2D)4p^3D^o$	17.02 ns	337.0531 nm(vac.)	

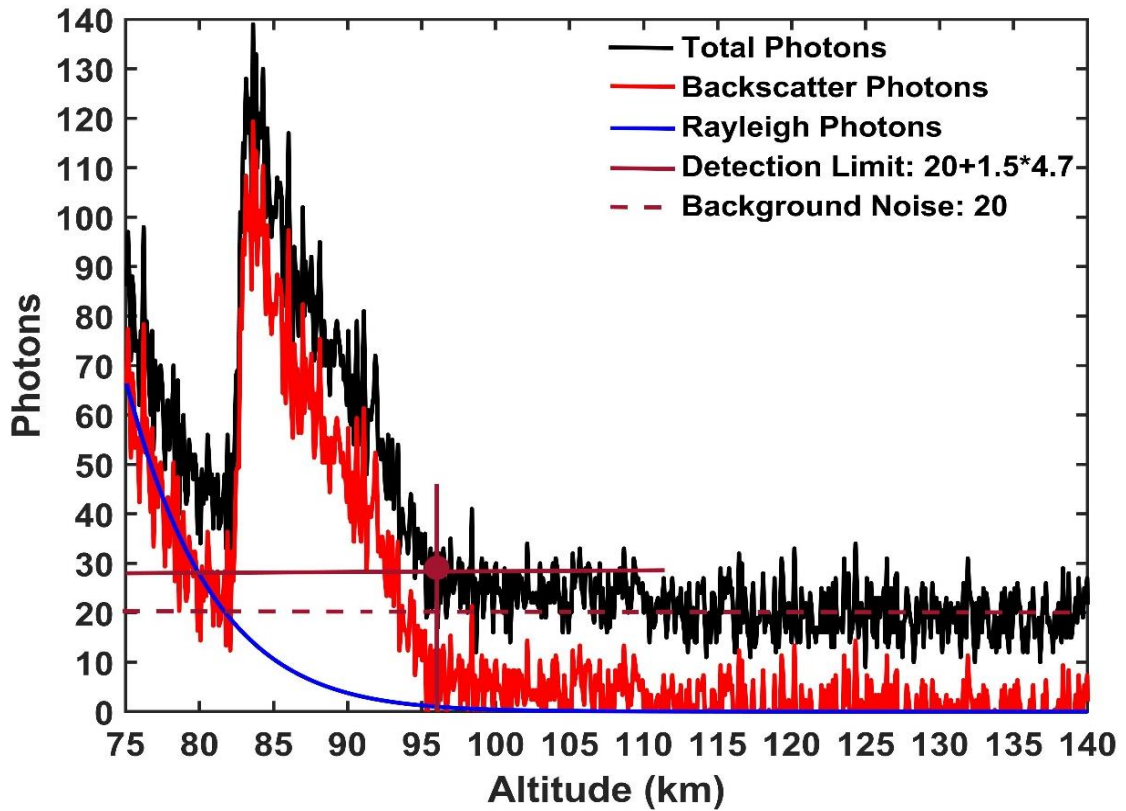
Transitions from $3d^9(^2D)4p^3D^o$				
Upper level	Lower level	Wavelength / nm (vac.)	Einstein coefficient/s ⁻¹	Branching fraction
$3d^9(^2D)4p^3D^o$	$3d^9(^2D)4s^3D_3$	339.3957	2.4×10^7	0.4085
$3d^9(^2D)4p^3D^o$	$3d^8(^3F)4s^2^3F_4$	337.0531	1.8×10^7	0.3064
$3d^9(^2D)4p^3D^o$	$3d^9(^2D)4s^3D_2$	347.3539	1.2×10^7	0.2043
$3d^9(^2D)4p^3D^o$	$3d^9(^2D)4s^1D_2$	380.8233	4.3×10^6	0.0732
$3d^9(^2D)4p^3D^o$	$3d^8(^3F)4s^2^3F_3$	352.9009	4.2×10^5	0.0072
$3d^9(^2D)4p^3D^o$	$3d^8(^3P)4s^2^3P_2$	711.2925	2.0×10^4	0.0003
$3d^9(^2D)4p^3D^o$	$3d^8(^3F)4s^2^3F_2$	364.2680	8.4×10^3	0.0001

1 We also calculated the branching ratios for the three transition lines
2 from the excited $3d^9(^2D)4p^3F_4$ state produced by pumping the $3d^9(^2D)4s^3D_3$
3 state at 341.5744 nm. The OD 5 interference filter with a bandwidth of 4
4 nm allows photons at 339.2016 nm to enter the PMT; moreover, the
5 transmittances of the OD 5 filter at the two wavelengths (341.5744 nm and
6 339.2016) are comparable (~93%, shown in Figure 12 (left panel)).
7 Therefore, the total number of photons recorded is the sum of the photons
8 at 341.5744 nm and 339.2016 nm. Figure 12 (right panel) shows that the
9 transmission of the OD 6 filter at 339.2016 nm is about 87%, and the
10 transmission at 341.5744 nm is only 1%. Therefore, the OD 6 filter only
11 transmits photons at 339.2016 nm when the nickel dye lidar wavelength is
12 341.5744 nm. The following experiment was therefore carried out in order
13 to determine the branching ratios for the three transition lines (341.5744
14 nm, 339.2016 nm, and 355.2551 nm).



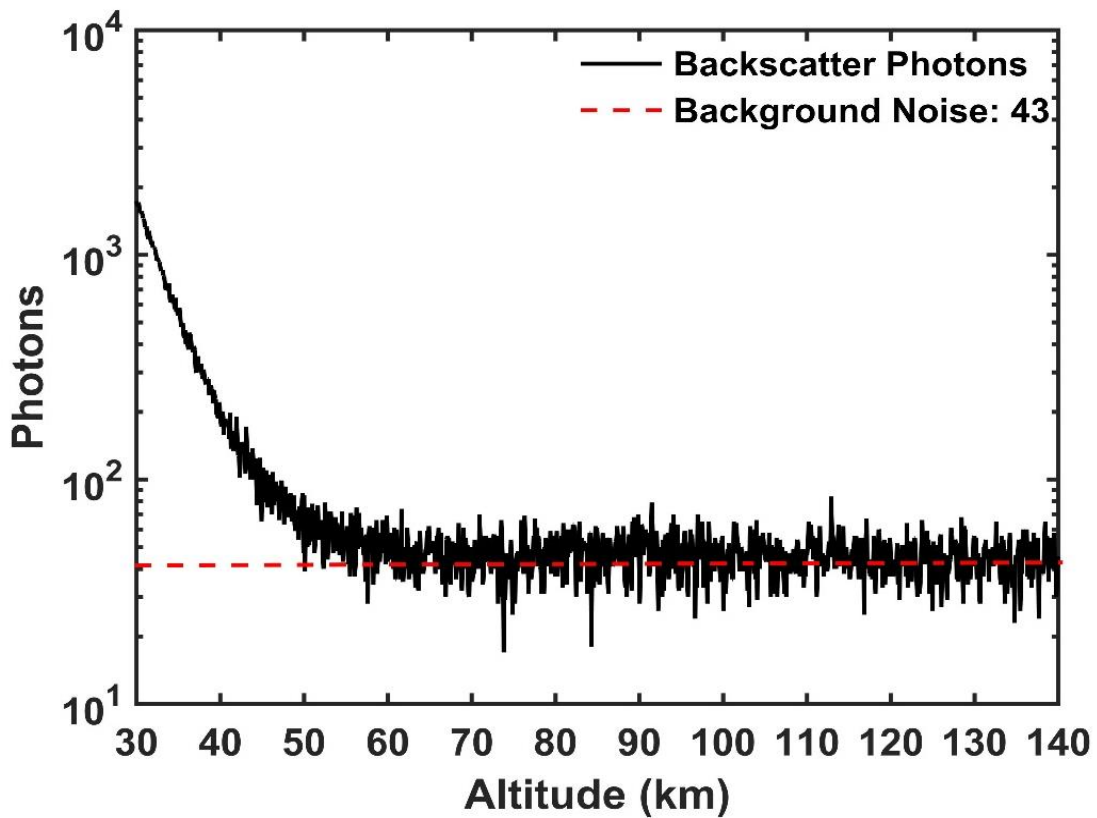
1
 2 Figure 12. Left panel: the transmittance of OD 5 filter at different wavelengths. Right panel: the transmittance of
 3 OD 6 filter at different wavelengths.

4 From 18:30 -19:00 UT on May 6, 2019, the 341.5744 nm laser beam
 5 was used to pump Ni atoms in the MLT layer, with the OD 5 filter in the
 6 lidar receiver. The OD 5 filter was then replaced with the OD6 filter, and
 7 keeping the same laser wavelength backscattered signal was collected from
 8 19:12 - 19:42 UT. The two lidar signals are presented in Figure 13 and
 9 Figure 14.



1
2
3
4

Figure 13. Lidar signal received through the OD 5 filter with the laser wavelength (at 341.5744 nm). The detection limit and the extrapolated Rayleigh background photons are showed. (Time resolution is 30 min, spatial resolution is 96 m).



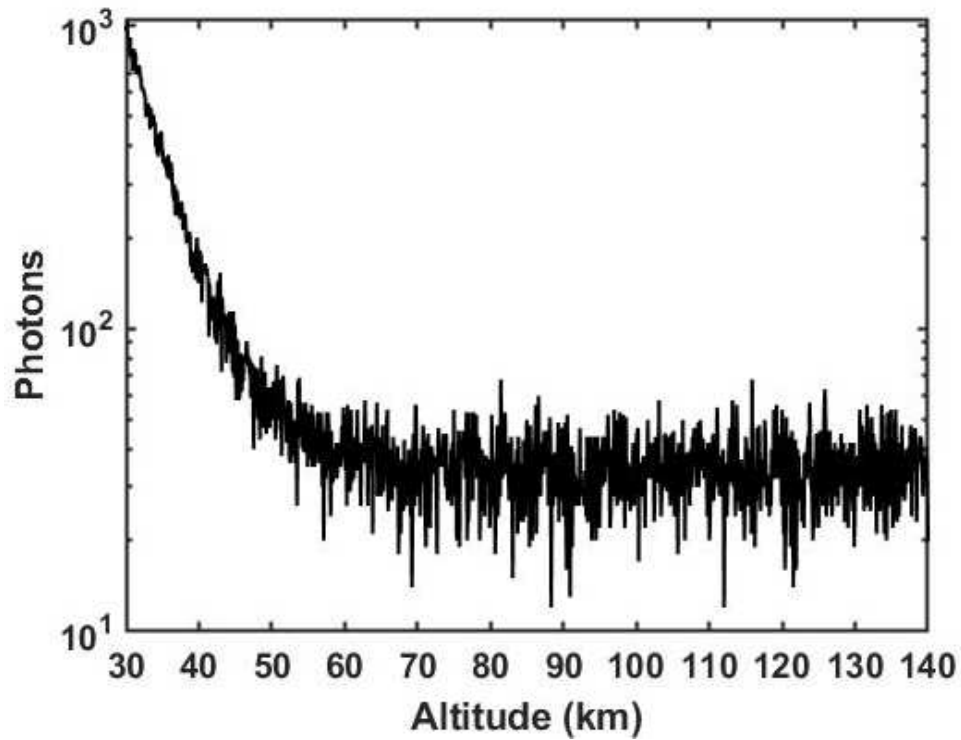
5
6

Figure 14. Backscatter photons received through the OD 6 filter with the laser wavelength (at 341.5744 nm).

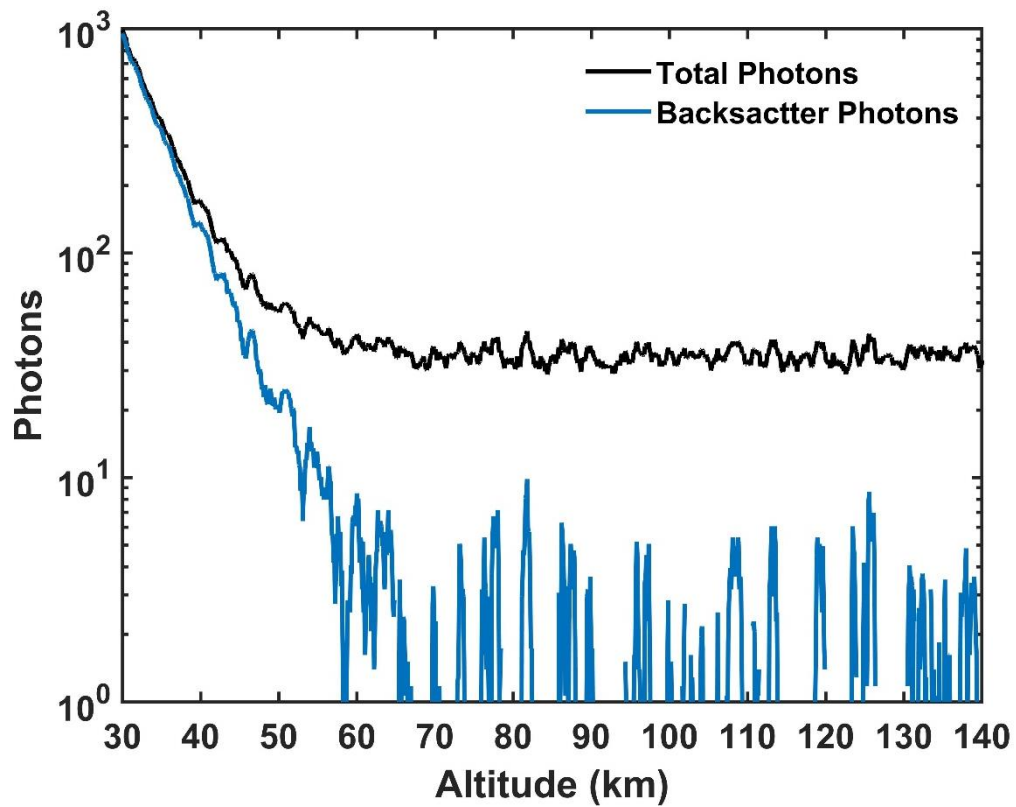
1 In the lidar signal obtained using the OD 5 filter we cannot determine
2 whether the photons above 100 km are signals or noise, so we only count
3 the number of photons above the detection limit shown in Figure 13. The
4 total number of photons at the two wavelengths (341.5744 nm and
5 339.2016 nm) in the 82 ~ 96 km range is 6712 photons (excluding
6 background noise and Rayleigh background signal). In comparison, 663
7 photons at 339.2061 nm were collected by the receiver using the OD 6
8 filter (Figure 14). Because the transmittance of the two filters at 339.2016
9 nm is different (OD 6: ~ 93%, OD 5: ~ 87%), we correct the received 663
10 photons: $663 \times \frac{0.93}{0.87} = 708$. The number of photons received with OD5 filter
11 at 341.5744 nm is therefore the difference: 6004 photons.

12 In addition, in order to determine the branching ratio of the transition
13 line $3d^9(^2D)4p^3F_4 \rightarrow 3d^8(^3F)4s^2^3F_3$, we deliberately used an OD 8 filter with
14 a high attenuation rate and a narrow bandwidth to receive echo photons
15 with a wavelength at 355.2551 nm. The OD 8 filter with a 1.2 nm FWHM
16 has a transmittance of greater than 80% at 355.2551 nm. The 341.5744 nm
17 laser beam was emitted and the OD 8 filter was used to receive the lidar
18 signal. The lidar signal is shown in Figure 15. In order to more accurately
19 determine whether there is a weak nickel signal in Figure 15, we smooth
20 the data and present the backscatter signal after removing background
21 noise in Figure 16. Clearly, the Ni echo photons with a wavelength at
22 355.2551 nm were not detected. This shows that the strength of the

- 1 $3d^9(^2D)4p^3F_4 \rightarrow 3d^8(^3F)4s^2^3F_3$ transition is very low, and the branching ratio
- 2 is very small. This corresponds to the literature value [30] (see Table. 2).



3
4 Figure 15 .Lidar signal through the OD 8 filter with the laser wavelength at 341.5744 nm. (Time resolution is 30
5 min; spatial resolution is 96 m).



6

1 Figure 16. Black line: the total backscatter photons in Figure 15 are smoothed by 10 points. Blue line: the
 2 backscattered photons after removing background noise from the smoothed data. (Time resolution is 30 min;
 3 spatial resolution is 96 m).

4 Therefore, the number of backscatter photons at 341.5744 nm and
 5 339.2016 nm can be used to estimate the branching ratio of the two
 6 transition lines $(3d^9(^2D)4p^3F \rightarrow 3d^9(^2D)4s^3D_3$ and $3d^9(^2D)4p^3F_4 \rightarrow$

7 $3d^8(^3F)4s^2\ ^3F_4)$. The branching ratios are $\frac{6004}{6712} \approx 0.8945$ (341.5744 nm)

8 and $\frac{708}{6712} \approx 0.1055$ (339.2016 nm). In addition, we consider the errors

9 from photon statistics. The photon counts uncertainty of the 6712 photons
 10 is 27 photons, the photon counts uncertainty of the 708 photons is 25
 11 photons. For the transition line $(3d^9(^2D)4p^3F \rightarrow 3d^9(^2D)4s^3D_3$ (341.5744

12 nm)), the branching ratio is between $\frac{(6712 + 27) - (708 - 25)}{6712 + 27} \approx 0.8986$

13 and $\frac{(6712 - 27) - (708 + 25)}{6712 - 27} \approx 0.8904$. Therefore, the error (from photon

14 statistics) of the branching ratio ($(3d^9(^2D)4p^3F \rightarrow 3d^9(^2D)4s^3D_3$ (341.5744
 15 nm)) is 0.0041. For the transition lines $(3d^9(^2D)4p^3F_4 \rightarrow 3d^8(^3F)4s^2\ ^3F_4$

16 (339.2016 nm)), the branching ratio is between $\frac{708 + 25}{6712 - 27} \approx 0.1096$ and

17 $\frac{708 - 25}{6712 + 27} \approx 0.1014$. The error (from photon statistics) of the branching

18 ratio ($(3d^9(^2D)4p^3F_4 \rightarrow 3d^8(^3F)4s^2\ ^3F_4$ (339.2016 nm)) is also 0.0041.

19 Finally, this gives $\frac{6004}{6712} \approx 0.8945 \pm 0.0041$ and

1 $\frac{708}{6712} \approx 0.1055 \pm 0.0041$, respectively, which are very similar to the values

2 listed in Table 2.

3 **6. Discussion and Conclusions**

4 A new lidar system for measuring atomic Ni in the MLT has been
5 developed at the Yanqing station ($40^\circ \text{N}, 116^\circ \text{E}$), near Beijing. Following
6 the earlier studies by Collins et al. [22] and Gerding et al. [23], we report
7 here measurements of the Ni layer at 40°N during 25 nights over 8
8 months. This demonstrates the stability of the system for making
9 continuous Ni measurements over an extended period, enabling the first
10 investigation of night-time and seasonal density variation of the Ni layer.

11 The performance of the Yanqing Ni lidar is enhanced in several ways
12 compared to the earlier studies: frequency-doubling near-IR laser radiation
13 confers several advantages over using an excimer laser-pumped dye laser
14 with a UV dye, as discussed in Section 2.2. Using a narrow bandwidth
15 interference filter also leads to a significant improvement in SNR.

16 The peak Ni density of nickel atoms reported by Collins et al. [22]
17 was $\sim 16,000 \text{ cm}^{-3}$, much larger than the value range of $280 \sim 450 \text{ cm}^{-3}$
18 reported by Gerding et al. [23]. As argued by Daly et al. [31], the very high
19 value – which is comparable to the peak Fe density – cannot be explained
20 in terms of the relative abundance of Ni and Fe in cosmic dust, which is
21 very similar to the relative abundances of Ni^+ and Fe^+ in the lower
22 thermosphere. The nightly-averaged Ni densities in the present study are

1 taken from lidar measurements at Yangqing between 3 April and 31
2 December 2019 (25 days in total): the peak density is about $100 \sim 460 \text{ cm}^{-3}$
3 ³, and the average column abundances varies from $(1.52 \text{ to} \sim 6.0) \times 10^8 \text{ cm}^{-2}$
4 ². The average peak density and the average column density abundance
5 over the 25 nights is $258 \pm 115 \text{ cm}^{-3}$ and $(3.0 \pm 1.4) \times 10^8 \text{ cm}^{-2}$, respectively,
6 which is similar to the results reported by Gerding et al. [23].

7 For the first time, we used the high altitude Ni lidar to determine the
8 branching ratios for three different optical transition from Ni in the
9 $3d^9(2D)4s^3D^3$ state (excited at 341 nm), and showed that these branching
10 ratios are very close to the theoretical values listed in Table 2.

11 Recently, a modelling study of the global Ni layer has been published,
12 where a full set of neutral and ion-molecule reactions involving Ni species
13 has been incorporated into the Whole Atmosphere Community Climate
14 (WACCM) model [31]. The results of the WACCM-Ni model are
15 generally in good agreement with the present study. A 3-fold increase in
16 the Ni column abundance is predicted from mid-summer to mid-winter at
17 40°N , which seems to be in good agreement with the present study (Figure
18 11). However, the modelled peak height is predicted to show little diurnal
19 variation, unlike the observations from Yanqing e.g. the very low peak
20 height around 78 km shown in Figure 8 after 16:00 UTC. This needs further
21 investigation. Nevertheless, the observed nightly average peak height
22 varied from 80 km to 88 km, which covers the range predicted by

1 WACCM-Ni [31]. The diurnal and seasonal variation of the Ni layer will
2 be compared in more detail with WACCM-Ni in a future study, once a full
3 year of Ni lidar measurements has been completed.

4 5 **Funding**

6 We thank the National Natural Science Foundation of China (41627804).
7 The work at Leeds was supported by the Natural Environment Research
8 Council (Grant NE/P001815/1).

9 **Acknowledgment**

10 We are very grateful to Xinzhao Chu, Chester S. Gardner and Chiao-Yao
11 She for their valuable suggestions on nickel detection technology. We also
12 very grateful to M. Gerding for his help in the density calculation and
13 Xinzhao Chu for her help with the “drag” problem (caused by Amplified
14 Spontaneous Emission (ASE)) of the dye laser. We appreciate the strong
15 support of National Space Science Center research fund for key
16 development directions, and the Specialized Research Fund for State Key
17 Laboratories of China. This research was also support by the Chinese
18 Meridian Project.

19 **Disclosures**

20 The authors declare no conflicts of interest.

21 **References**

22 [1] J. M. C. Plane, W. Feng, and E. C. M. Dawkins, “The Mesosphere and Metals: Chemistry and
23 Changes,” *Chem. Rev.* 115(10):4497-541(2015). <https://doi.org/10.1021/cr500501m>.

- 1 [2] J. Y. Xu, A. K. Smith, "Perturbations of the sodium layer: Controlled by chemistry or dynamics?"
2 *Geophys. Res. Lett.* 30, 2056(2003). <https://doi.org/10.1029/2003GL018040>.
- 3 [3] C. Ban, T. Li, X. Fang, X. K. Dou, and J. G. Xiong, "Sodium lidar-observed gravity wave
4 breaking followed by an upward propagation of sporadic sodium layer over Hefei, China," *J.*
5 *Geophys. Res.* 120, 7958-7969(2015). <https://doi.org/10.1002/2015JA021339>.
- 6 [4] X. G. Cai, T. Yuan, and J. Vincent Eccles, "A Numerical Investigation on Tidal and Gravity
7 Wave Contributions to the Summer Time Na Variations in the Midlatitude E Region," *J. Geophys.*
8 *Res.* 122, 10577-10595(2017). <https://doi.org/10.1002/2016JA023764>.
- 9 [5] C. J. Heinselman, J. P. Thayer, and B. J. Watkins, "A high latitude observation of sporadic
10 sodium and sporadic E layer formation," *Geophys. Res. Lett.* 25, 3059–3062 (1998). [https://doi.org/](https://doi.org/10.1029/98GL02215)
11 [10.1029/98GL02215](https://doi.org/10.1029/98GL02215).
- 12 [6] C. S. Gardner, T. J. Kane, D. C. Senft, J. Qian, and G. C. Papen, "Simultaneous observations of
13 sporadic E, Na, Fe, and Ca⁺ layers at Urbana, Illinois: three case studies," *J. Geophys. Res.* 98,
14 16865–16874 (1993). <https://doi.org/10.1029/93JD01477>.
- 15 [7] M. K. Ejiri, T. Nakamura, T. T. Tsuda, T. Nishiyama, M. Abo, C.-Y. She, M. Nishioka, A. Saito,
16 T. Takahashi, and K. Tsuno, "Observation of synchronization between instabilities of the sporadic
17 E layer and geomagnetic field line connected F region medium scale traveling ionospheric
18 disturbances," *J. Geophys. Res.* 124, 4627–4638 (2019). <https://doi.org/10.1029/2018JA026242>.
- 19 [8] Y. Xia, L. Du, X. Cheng, F. Li, J. Wang, Z. Wang, Y. Yang, X. Lin, Y. Xun, S. Gong and G.
20 Yang, "Development of a solid-state sodium Doppler lidar using an all-fiber-coupled injection
21 seeding unit for simultaneous temperature and wind measurements in the mesopause region," *Opt.*
22 *Expr.*, 5, 25(2017). <https://doi.org/10.1364/OE.25.005264>.
- 23 [9] X. Hu, Z. A. Yan, S. Y. Guo, Y. Cheng, and J. Gong, "Sodium fluorescence Doppler lidar to
24 measure atmospheric temperature in the mesopause region," *Chin. Sci. Bull.* 56(4-5), 417–
25 423(2011). <https://doi.org/10.1007/s11434-010-4306-x>.
- 26 [10] T. Li, X. Fang, W. Liu, S.-Y. Gu, and X. Dou, "Narrowband sodium lidar for the measurements
27 of mesopause region temperature and wind," *Appl. Opt.* 51(22), 5401–5411 (2012). [https://doi.org/](https://doi.org/10.1364/AO.51.005401)
28 [10.1364/AO.51.005401](https://doi.org/10.1364/AO.51.005401).
- 29 [11] M. R. Bowman, A. J. Gibson, and M. C. W. Sandford, "Atmospheric sodium measured by a
30 tuned laser radar," *Nature* 221, 456–457(1969). <https://doi.org/10.1364/AO.51.005401>.
- 31 [12] A. J. Gibson and M. C. W. Sandford, "The seasonal variation of the night-time sodium layer,"
32 *J. Atmos. Terr. Phys.* 33, 1675–1684 (1971). [https://doi.org/10.1016/0021-9169\(71\)90215-7](https://doi.org/10.1016/0021-9169(71)90215-7).
- 33 [13] R. L. Collins, T. J. Hallina, R. W. Smith, and G. Hernandez, "Lidar observations of a large
34 high-altitude sporadic Na layer during active aurora," *Geophys. Res. Lett.* 23, 3655–3658 (1996).
35 <https://doi.org/10.1029/96GL03337>.
- 36 [14] Y. Xun, G. Yang, C.-Y. She, J. Wang, L. Du, Z. Yan, Y. Yang, X. Cheng, and F. Li, "The first
37 concurrent observations of thermospheric Na layers from two nearby central midlatitude lidar
38 stations," *Geophys. Res. Lett.* 46, 1892–1899 (2019). <https://doi.org/10.1029/2018GL081645>.
- 39 [15] J. Wang, Y. Yang, X. Cheng, G. Yang, S. Song, and S. Gong, "Double sodium layers
40 observation over Beijing, China," *Geophys. Res. Lett.* 39(15)(2012).
41 <https://doi.org/10.1029/2012GL052134>.
- 42 [16] U. von Zahn, J. Höffner, "Mesopause temperature profiling by potassium lidar," *Geophys. Res.*
43 *Lett.* 23(2): 141-4(1996). <https://doi.org/10.1029/95GL03688>.
- 44 [17] Z. Wang, G. Yang, J. Wang, Y. Chuan, Y. Yang, J. Jiao, L. Du, X. Cheng, and C. Wang,
"Seasonal variations of meteoric potassium layer over Beijing (40.41°N, 116.01°E)," *J. Geophys.*

1 Res. 122(2)(2017). <https://doi.org/10.1002/2016JA023216>.

2 [18] M. Gerding, M. Alpers, J. Höffner, and U. von Zahn, “Sporadic Ca and Ca⁺ layers at mid-
3 latitudes: Simultaneous observations and implications for their formation,” *Annales Geophysicae*.
4 19: 47-58(2001). <https://doi.org/10.5194/angeo-19-47-2001>.

5 [19] S. Raizada, C. A. Tepley, N. Aponte, and E. Cabassa, “Characteristics of neutral calcium and
6 Ca⁺ near the mesopause, and their relationship with sporadic ion/electron layers at Arecibo,”
7 *Geophys. Res. Lett.* 38, L09103 (2011). <https://doi.org/10.1029/2011GL047327>.

8 [20] J. S. Friedman, X. Chu, C. G. M. Brum and X. Liu, “Observation of a thermospheric descending
9 layer of neutral K over Arecibo,” *J. Atmos. Terr. Phys.* 104:253-269(2013).
10 <https://doi.org/10.1016/j.jastp.2013.03.002>.

11 [21] S. Raizada, C. M. Brum, C. A. Tepley, Jens Lautenbach, J. S. Friedman, John D. Mathews, F.
12 T. Djuth, and Caitlin Kerr, “First simultaneous measurements of Na and K thermospheric layers
13 along with TILs from Arecibo,” *Geophys. Res. Lett.* 42, 10,106-10,112(2015).
14 <https://doi.org/10.1002/2015GL066714>.

15 [22] R. L. Collins, J. Li, and C. M. Martus, “First lidar observation of the mesospheric nickel layer,”
16 *Geophys. Res. Lett.* 42, 665–671(2015). <https://doi.org/10.1002/2014GL062716>.

17 [23] M. Gerding, S. Daly, and J. M. C. Plane, “Lidar Soundings of the Mesospheric Nickel Layer
18 Using Ni(³F) and Ni(³D) Transitions,” *Geophys. Res. Lett.* 46(2018).
19 <https://doi.org/10.1029/2018GL080701>.

20 [24] C. Wang, “New chains of space weather monitoring stations in China,” *Space Weather* 8, 1-
21 5(2010). <https://doi.org/10.1029/2010SW000603>.

22 [25] G. Megie, F. Bos, J. Blamont, and M. Chanin, “Simultaneous nighttime lidar measurements
23 atmospheric sodium and potassium,” *Planet. Space Sci.* 26, 27-35(1978).
24 [https://doi.org/10.1016/0032-0633\(78\)90034-X](https://doi.org/10.1016/0032-0633(78)90034-X).

25 [26] X. Chu and G. C. Papen, “Resonance fluorescence lidar for measurements of the middle and
26 upper atmosphere,” in *Laser Remote Sensing*, T. Fujii and T. Fukuchi, eds. (CRC Press, 2005), pp.
27 179–432. <https://doi.org/10.1201/9781420030754.ch5>.

28 [27] J. M. Picone, A. E. Hedin, D. P. Drob, and A. C. Aikin, “NRLMSISE-00 empirical model of
29 the atmosphere: Statistical comparison and scientific issues,” *J. Geophys. Res.* 107(A12),
30 1468(2002). <https://doi.org/10.1029/2002JA009430>.

31 [28] F. Cairo, F. Congeduti, M. Poli, S. Centurioni, G. Di Donfrancesco, “A survey of the signal -
32 induced noise in photomultiplier detection of wide dynamics luminous signals,” *REV. SCI.*
33 *INSTRUM.* 67(9):3274 – 3280(1996). <https://doi.org/10.1063/1.1147408>.

34 [29] Q. Gao, X. Chu, X. Xue, X. Dou, T. Chen, J. Chen, “Lidar observations of thermospheric Na
35 layers up to 170km with a descending tidal phase at Lijiang (26.7°N, 100.0°E), China,” *J. Geophys.*
36 *Res.* 120, 9213–9220(2015). <https://doi.org/10.1002/2015JA021808>.

37 [30] A. Kramida, Y. Ralchenko, J. Reader, and NIST ASD Team. NIST Atomic Spectra Database
38 (version 5.5.6), [Online]. Available: <https://physics.nist.gov/asd>. National Institute of Standards and
39 Technology, Gaithersburg, MD(2018).

40 [31] S. M. Daly, W. Feng, T. P. Mangan, M. Gerding, and J. M. C. Plane, “The meteoric Ni layer
41 in the upper atmosphere,” *J. Geophys. Res.* 125(2020). <https://doi.org/10.1029/2020JA028083>.